

Design and performance of a high rate, high angular resolution beam telescope used for crystal channeling studies

M. Pesaresi, W. Ferguson, J. Fulcher, G. Hall, M. Raymond, M. Ryan, O. Zorba

Blackett Laboratory, Imperial College London

SW7 2AZ, UK

E-mail: mark.pesaresi@imperial.ac.uk

ABSTRACT:

A charged particle telescope has been constructed for data taking at high rates in a CERN 400 GeV/c proton beam line. It utilises ten planes of silicon microstrip sensors, arranged as five pairs each measuring two orthogonal coordinates, with an active area of $3.8 \times 3.8 \text{ cm}^2$. The objective was to provide excellent angular and spatial resolution for measuring the trajectories of incident and outgoing particles. The apparatus has a long baseline, of approximately 10 m in each arm, and achieves an angular resolution in the incoming arm of $2.8 \mu\text{rad}$ and a total angular resolution on the difference of the two arms of $5.2 \mu\text{rad}$, with performance limited by multiple scattering in the sensor layers. The sensors are instrumented by a system based on the CMS Tracker electronic readout chain, including analogue signal readout for optimal spatial resolution. The system profits from modified CMS software and hardware to provide a data acquisition capable of peak trigger rates of at least 7 kHz. We describe the sensor readout, electronic hardware and software, together with the measured performance of the telescope during studies of crystal channeling for the UA9 collaboration. Measurements of a previously unobserved periodic movement of the beam are also presented and the significance of such an effect for precise studies such as for channeling is discussed.

KEYWORDS: silicon microstrips; beam telescope; APV25; crystal channeling, UA9.

Contents

1. Introduction	1
1.1 Coordinate system	2
2. Telescope Hardware	2
2.1 Sensors	3
2.2 Front end hybrids	3
2.3 Optical link	4
2.4 Readout and control system	4
2.5 XY plane construction	6
3. Data Acquisition	6
3.1 Hardware architecture	7
3.2 Software and run control	8
3.3 Data throughput	10
3.4 Data storage and formatting	11
4. Results	11
4.1 Detector setup and performance	12
4.2 Track reconstruction and telescope performance	15
4.3 Beam quality and observation of channeling	18
5. Conclusions	20

1. Introduction

The original motivation for the development of this apparatus was in anticipation of studies of future detector modules for upgrades of the CMS Tracker[1] to meet the requirements of high luminosity operation of the Large Hadron Collider (LHC) in the next decade. Several new module types are under study and it will be essential to evaluate them under the widest range of possible operating conditions, including before and after irradiation. Studies will include operation at the data taking rates to be encountered in the experiment, which is important to identify possible subtle system features which are often not easily identified at lower rates. This requires 40 MHz clocked operation with up to 100 kHz triggered readout with minimal deadtime.

During the course of planning the telescope for these studies it was realized that the apparatus could also be deployed to contribute to evaluations of crystal channeling of high momentum protons. Channeling of charged particles in a bent crystal has been used as a technique to steer ultra-relativistic beams and developments are under way by the UA9 collaboration to demonstrate

the technique could improve the collimation of proton and heavy ion beams at the LHC[2]. Measurements of suitable crystals are being carried out in the SPS ring as well as in a fixed target experiment in the CERN North experimental area. The study of channeling phenomena requires very accurate angular alignment of the silicon crystals with respect to the beam as the critical angle for channeling, i.e. the angular acceptance of incident particles with respect to the crystalline planes, is of the order of $10\ \mu\text{rad}$ for 400 GeV/c protons.

A narrow, low divergence 400 GeV/c proton beam is available in the external H8 beamline of the CERN SPS. Silicon crystals of various types are placed on a high precision goniometer at the centre of the apparatus and slowly rotated to align them to the correct orientation for proton channeling. Tracking of the incident and outgoing protons is required to identify when channeling occurs and to measure the efficiency. Silicon microstrip detectors are well suited for the tracking, being relatively low mass and with high spatial precision. They can also be read out at high rates, which can speed up the measurements and, in particular, allow rotational scans of the goniometer to be carried out quickly. The total angular resolution of the telescope, i.e. the resolution on the proton deflection measurement, should be of a few μrad . In addition, an angular resolution of the incident arm must be minimised in order to select tracks incident on the crystal within the channeling acceptance.

In practice, exploiting the time structure of the SPS beam means taking several thousand events in a 10 s spill, followed by a ~ 35 s gap during which the goniometer moves to the next position. Since the typical goniometer step is $\sim 2\ \mu\text{rad}$ it is highly desirable to achieve sufficient statistical precision in a single spill both to speed up the search and to avoid temporal variations over the angular scan (up to ~ 0.3 mrad). Previous measurements in the same beamline[3] acquired data over many spills. The CMS tracker electronic system design[4] is well adapted to the challenge of speeding up the UA9 H8 measurements due to its requirements for data taking at the LHC 40 MHz beam crossing rate, Level 1 trigger readout at up to 100 kHz and minimal deadtime of at most about 1%.

1.1 Coordinate system

In the description which follows, a left-handed coordinate system is adopted with the z-axis the approximate direction of the beam and x- and y- directions referring to the horizontal and vertical displacements. Hence the measurement stations are referred to as XY planes. The crystals used for channeling studies are usually oriented so that the expected displacement is in the horizontal plane and so the angular scan is about a vertical axis.

2. Telescope Hardware

The telescope readout system is based on components developed for the CMS silicon microstrip tracker[1] while sensors were chosen because of ready availability and proven quality, with expected spatial precision compatible with the requirements. The same type of sensors have been previously used by others in a compact telescope to study the performance of irradiated devices[5]. The APV25 was also adopted for the sensor readout by the authors of [5], but used early prototypes of the CMS off-detector readout hardware. Here final components of the full CMS tracker readout chain were used, including optical signal transmission and off-detector front end data acquisition

(DAQ) components, to maximise rate capability. For maximum flexibility in the configuration of the telescope each XY plane was constructed as a separate instrument. Figure 1 shows a functional block diagram of a plane. Five were made, each consisting of two microstrip sensors mounted orthogonally.

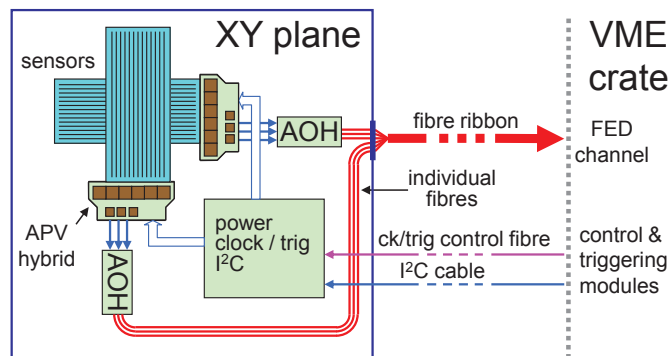


Figure 1. Functional block diagram of an XY plane.

2.1 Sensors

The sensors used are identical to those described in [5]; they are single-sided silicon strip detectors fabricated by Hamamatsu Photonics (HPK) on high resistivity float-zone material, originally procured for application in the DØ experiment[6] for the proposed Run IIb at the FNAL Tevatron. They are AC coupled, nominally $320\ \mu\text{m}$ thick, and consist of 639 strips (98 mm long) on a $60\ \mu\text{m}$ readout pitch, with a floating intermediate strip. Typically the sensors have total leakage currents over a wide range of voltages up to 500 V of 100-200 nA and full depletion at 100 V, with good uniformity in the sample of sensors available. The individual strips also have excellent behaviour; the assembled modules displayed no dead strips or excessive noise indicating extremely good quality sensors.

The active area of the XY plane, where the two sensors overlap, is $38 \times 38\ \text{mm}^2$. During this study the sensors were biased to 150 V.

2.2 Front end hybrids

The sensors are read out by APV25 chips[7] mounted on hybrids developed for use in the Inner Barrel of the CMS Tracker. The APV25 is a 128 channel $0.25\ \mu\text{m}$ CMOS chip designed specifically for use in CMS for silicon microstrips with capacitances of 10-20 pF, and is well-suited to the sensors used here. The front-end amplifier produces a CR-RC shaped pulse with a peaking time of 50 ns, and consecutive samples of the pulse shape are continuously stored in an analogue pipeline memory every 25 ns using a 40 MHz clock. The operational mode of the APV25 chip, and bias settings, are programmable via an I²C interface; more details can be found in [7]. For this application the chip was configured to operate in peak mode, where a single sample (for every channel) is retrieved from the pipeline following an external trigger, and an output data frame is produced containing the analogue samples from all 128 channels. Accessing the analogue memory is achieved by write and trigger pointers, with a programmable delay (latency) between them,

such that when a trigger is applied the corresponding data sample which is retrieved was stored a latency period previously. For a telescope application this feature can be used to accommodate all the delays (signal propagation, decision taking) associated with generating a trigger from a beam particle traversing a scintillator and transmitting it to the front end to initiate readout.

The front end hybrids used have six APV25 chips. Five are used to read out the 639 strips (with one unbonded channel) and one chip is unused. Three other ancillary chips present on the front end hybrids are a detector control unit chip (DCU), a phase-locked loop chip (PLL) and an APVMUX chip. The DCU can be used to monitor currents, voltages and temperatures on the front end hybrid. The PLL recovers the 40 MHz clock and trigger signals from a combined input signal, where the trigger is encoded as a missing clock pulse, and transmits them to the APV25 chips. The APVMUX chip combines the outputs of two APV25 chips onto a single line by a simple 40 MHz multiplexing operation, a feature adopted in the CMS Tracker to save on the number of readout links required. Each front end hybrid therefore provides three output lines to carry the data from six APV25 chips.

2.3 Optical link

In CMS the front end signals are transmitted optically off-detector to the front end of the DAQ system. The optical signals are then converted back to electrical in a VME module called a Front End Driver (FED)[8]. Optical transmission avoids the mass associated with the cables required for long distance electrical transmission and also has the advantage of immunity to electrical interference. For each front end hybrid an analogue optical hybrid (AOH)[9] converts the three electrical signals to optical levels, using a Fabry-Perot edge-emitting semiconductor laser operating at 1310 nm wavelength, which are transmitted on single mode fibres. Each XY plane thus has 6 individual optical fibre connectors whose outputs are combined into a single fibre ribbon cable for transferring the signals over long distances. The ribbon cable can be constructed in a ruggedized form.

2.4 Readout and control system

Figure 2 shows a block diagram of the telescope including details of the control and data acquisition system hardware. Each XY plane has an analogue optical fibre ribbon output, a single digital control fibre input, and an electrical I²C bus input for slow control and monitoring. The control and DAQ system is housed remotely in a VME crate, and the operational state of the DAQ and front end is set up by a control PC via the CAEN V2718 crate controller. The functionality of the system can be explained by considering the sequence of operations following the passage of a charged particle through the telescope.

A scintillator-photomultiplier system provides an event trigger to the trigger logic module in the remote VME crate when a beam particle traverses the telescope planes. The trigger logic module will pass the trigger on to the sequencer module if the DAQ busy veto input is not active. When triggered, the sequencer module waits for a programmable delay before issuing a 25 ns trigger pulse to the electro-optical interface module. The programmable delay (25 ns resolution) must be adjusted in conjunction with the programmed latency in the APV25 chips, so that the trigger eventually arriving back at the front end is correctly timed to correspond to the peak of the pulse stored in the APV25 pipeline.

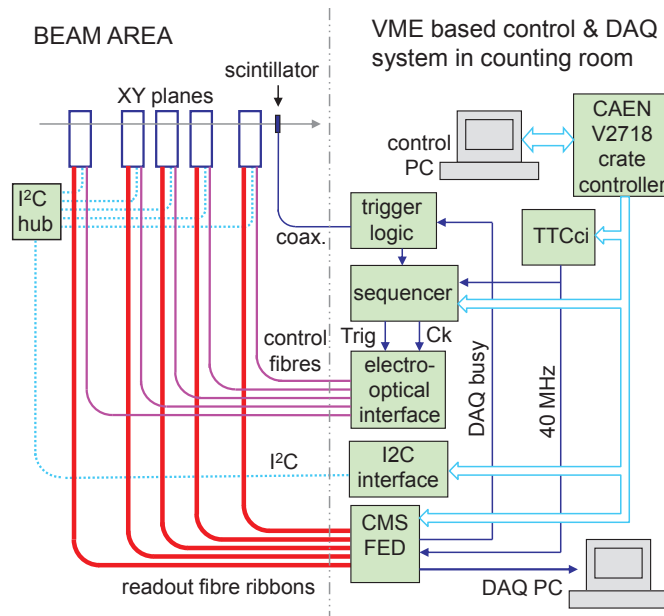


Figure 2. Functional block diagram of the telescope including readout and control system.

In the electro-optical interface module the trigger pulse is encoded into the 40 MHz clock as a missing pulse, and the resulting signal is fanned out and converted to optical signals which are then transmitted to the front end XY planes. The XY planes then produce their data frames which arrive back at the FED where optical signals are converted back to electrical and digitized.

Depending on how it is configured, the FED can provide raw data, which can be accessed via the VME crate controller, or can process the data by subtracting pedestals, subtracting any common mode effects, looking for signals above a programmable threshold (hits), and subsequently transmitting a data package containing the hits via a fast serial link to a separate external DAQ PC system. Higher speed is offered by the second, zero-suppressed, operational mode. Depending on trigger rate, data volumes and how fast the external DAQ PC can accept data, the FED can assert the DAQ busy signal to the trigger module to stop accepting triggers if internal buffers are close to full.

A master 40 MHz clock reference is provided to the control and DAQ system (sequencer and FED) by a CMS-specific timing, trigger and control VME module, the TTCci [10], and it is this clock which determines the sampling time in the APV25 chips. The beam arrival time is asynchronous, but the relatively long APV25 amplifier pulse shape means that there will always be a sample sufficiently close to the maximum signal amplitude.

A VME to I²C interface module provides the slow control path for accessing the I²C registers in the APV25, DCU, PLL and APVMUX and laser driver chips in the front end hybrids and AOH modules in the XY planes. The single I²C bus to the front end is fanned out by a custom I²C hub close to the XY planes. An initial I²C transaction selects which XY plane bus to activate for subsequent transactions. The I²C signalling is implemented electrically, and the bus speed is limited to 10 kHz to ensure reliable operation over relatively long distances. The I²C bus is opto-

isolated at the I²C hub input and the fanned out busses are further opto-isolated as they enter the XY plane enclosures. Each XY plane has its own individual high (sensor bias) and low voltage supplies. Since fast control and readout are also implemented optically, the planes are electrically isolated from the control and DAQ system, and from each other. This leads to a robust system with good immunity to electrical interference which can often be present in test beam environments.

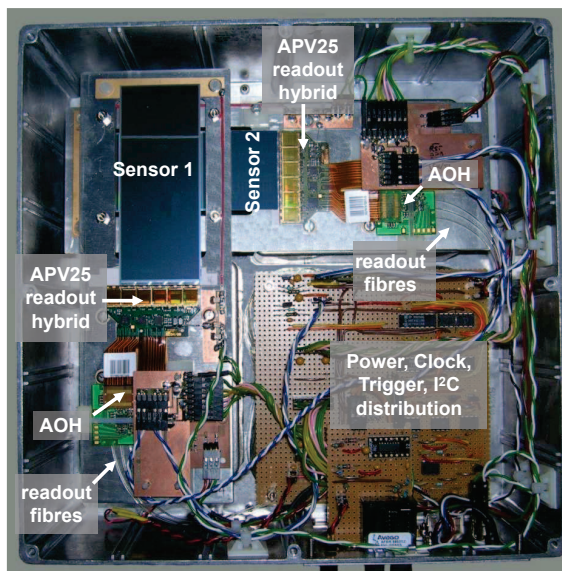


Figure 3. Photograph of the inside of an XY plane.

2.5 XY plane construction

Figure 3 shows a photograph of the internal construction of an XY plane with some of the component parts labelled. The planes are assembled in 25 cm × 25 cm × 10 cm, off-the-shelf, diecast boxes. The two orthogonal sensors can be seen with the readout hybrids, AOH modules and readout fibres, and the power, clock, trigger and I²C interface circuitry. Two XY planes, one rotated 45° with respect to the other, can be seen in Figure 4. The plane in the background is shown before a window has been installed, and one of the sensor planes can be seen through the opening. The plane in the foreground has its 30 μm thick aluminium foil window in place, and a second identical window is located in the rear face. In Figure 3 each sensor and associated readout hybrid is mounted on an aluminium alloy plate which is cooled by Peltier elements mounted underneath. The hot side of the Peltier devices is cooled by a small fan and these and their associated ventilation grills can be seen in Figure 4. The temperature of each sensor plate is sensed and the Peltier current is adjusted automatically by a microcontroller to keep the temperature stable at 20°C, independent of external environmental variations.

3. Data Acquisition

For measurements of crystal channeling, the principal objective is to perform angular scans of a crystal mounted on the goniometer in order to identify the correct orientation for channeling and



Figure 4. Photograph of two XY planes.

to take sufficient data around that position. The beam provided in the CERN H8 area is ejected with a time structure consisting of a flat top when particles are present, lasting about 10 s, followed by about 35 s of no beam. It is convenient therefore to change the goniometer angle in steps with adjustment taking place in the interval when no particles are present. The data capture rate must also be high enough to record enough events, typically a few thousand at each angular position, in order to provide adequate statistics within a reasonable time.

The Data Acquisition (DAQ) system is required to receive data from the telescope front end, format it for storage and provide online monitoring to confirm data quality. In order to permit an automated scan procedure to find the channeling orientation, the DAQ must also interface with the goniometer to control its positioning and record its coordinates in the data stream. The peak trigger rate is limited to 40 kHz within the sequencer in order to prevent buffer overflows in the front end APVs, although this could be increased to 140 kHz (peak) with buffer emulation logic. The important factors to consider when designing such a high rate DAQ system are event size, bandwidth bottlenecks, particle spill structure and period as well as available memory, buffer sizes, computational power and disk write speeds. When considering these parameters it was clear that a subset of the existing hardware designed for the CMS Tracker DAQ[11] was capable of achieving such a goal and could later be expanded relatively easily to achieve higher rates. The following section describes the architecture of the DAQ hardware and software and subsequent data path, formatting and storage.

3.1 Hardware architecture

The hardware of the system is developed around the CMS Tracker Front End Driver (FED)[8], which is responsible for the capture, digitization, processing and packaging of the analogue optical signals from the front end APV25 chips. The assembled event fragments are then shipped out over one of two readout routes: VME or a custom 64-bit width (80 MHz) short link standard (S-Link64)[12]. The DAQ architecture has been proven to run at data taking rates in excess of

100 kHz for the whole CMS detector. In CMS, event fragments are merged from multiple FEDs and processed on a large computer farm (>1000 CPUs) to select the most interesting events to be written to hard storage at a rate of 200-300 Hz and event size of ~ 1 MB. In contrast, for the beam telescope it is required to write all events to disk hence consideration of the processing and storage rate is important despite the much smaller event size.

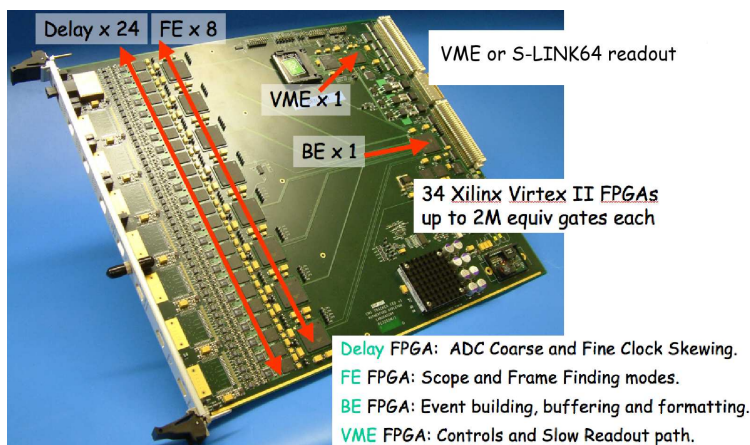


Figure 5. Photograph of a CMS Tracker FED. It is a 9U format VME board whose principal features are identified on the photograph.

The telescope system corresponds to only $\sim 0.1\%$ of the channels of the CMS Tracker. Keeping the basic functionality of the original system for this number of channels requires only a single FED. Figure 5 shows an annotated photograph of a Tracker FED. One FED contains 96 analogue optical inputs with individually adjustable gain settings and clock delay settings. It requires an optical clock and trigger synchronised with the signals from the front end modules. Part of the commissioning of this system requires that these signals be correctly timed in and that the delays due to cable length differences are taken into account by adjusting the clock delay FPGAs on the FED for every channel.

Data are transferred using the S-Link64 interface which substantially increases the readout rate compared with VME. A FEDKit[13] PCI card is installed in a DAQ PC and receives the S-Link data directly from the FED. This bypasses the requirement for the gigabit optical network fabric and associated modules used in CMS[14]. A large area of physical memory is reserved in the DAQ PC to buffer the data where it is directly accessed by the online software before it is cleared. To prevent overflows in the S-Link buffer, the interface automatically exerts backpressure on the FED until the FED buffers are occupied, at which point the DAQ busy veto signal is asserted and triggers are blocked at the trigger logic module. The veto is applied until the occupancies of all buffers in the readout chain fall below a nominal threshold.

3.2 Software and run control

The software is mainly written in C++ Object Oriented Classes with some supporting applications written in Java such as the Run Control Interface. The framework of the software is based upon the XDAQ[15] distributed architecture. Figure 6 is a schematic of the DAQ software.

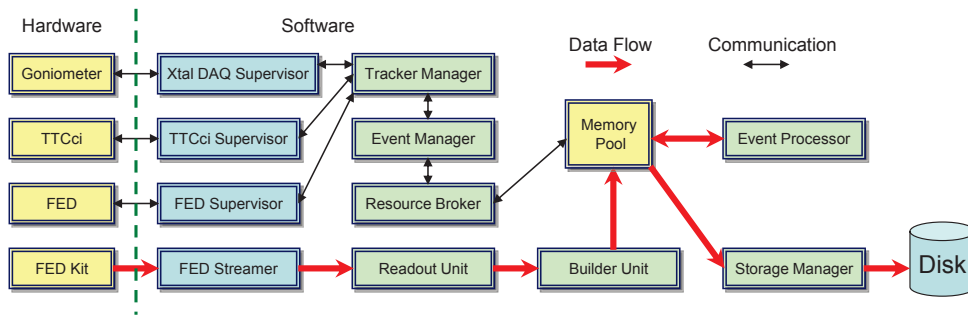


Figure 6. First version of DAQ online software employing only one Event Processor.

The software can be divided up into three main parts: DAQ online, run control user interface and data analysis. The DAQ online software is responsible for configuration and control of the run parameters of the DAQ and the parameters of the FED. The *Fed Supervisor* class is responsible for configuration, operation and monitoring of the FED (as well as for readout of the FED over VME if required). The *Tracker Supervisor* is responsible for the management of run parameters such as number of events per spill, monitoring requests to the FED and other applications and the communication of trigger tokens to the DAQ *Event Manager*. The *Readout Unit* is responsible for transfer of data from the FEDKit memory space to the *Resource Broker* buffers. The *Resource Broker* is responsible for management of the memory where the reconstruction of events by the *Event Processor* (EP) is performed. It also forwards events to the *Storage Manager* (SM), which is responsible for compressing and storing the data to disk. The EP is a software component used to unpack, format and repack the raw data for either online or offline analysis as well as for high level filtering and event selection.

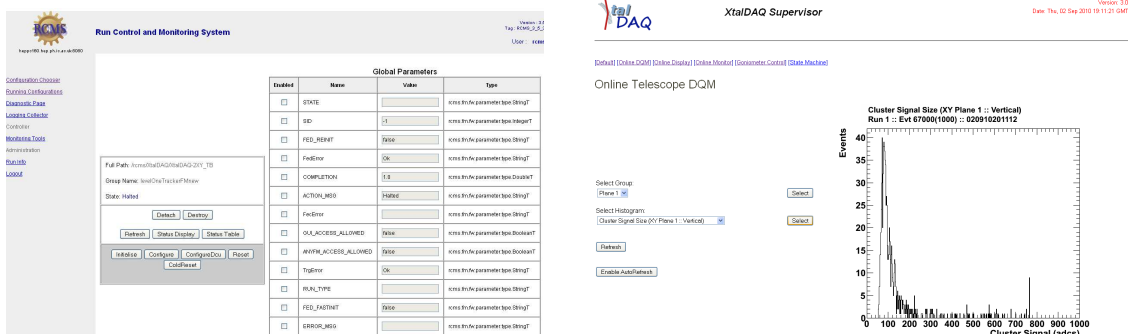


Figure 7. The DAQ is controlled using the CMS XDAQ Run Control interface (left) to start and stop runs. Results of real time data reconstruction and analysis are displayed in the web browsable XtalDAQ Supervisor interface (right).

The user interface as shown in Figure 7 is the standard implementation of the CMS XDAQ Run Control which provides a web page interface where the user can select, from a list of DAQ

operations, the specific configuration to be instantiated for a given run. A set of dynamic web pages provide important monitoring information and statistics such as number of events taken, amount of data passing through the DAQ and the total amount of data saved to disk. More advanced monitoring pages are also available and can display real time histograms of interesting quantities for data quality monitoring such as beam profiles, sensor efficiencies and cluster sizes and signals. In addition, results of prompt analyses can be provided including calculations of deflection angles due to crystal channeling.

Due to the nature of the XDAQ architecture it is possible to run the DAQ in many different configurations to try to optimize the efficiency of the overall system. An example schematic shown in Figure 8 provides a system capable of supporting peak trigger rates up to 40 kHz. The most serious bottleneck is due to the overhead in processing the events within the EP. By increasing the number of EPs from one to 8, a factor of 8 in the event rate is gained providing there are sufficient CPU cores on which to run the individual EPs.

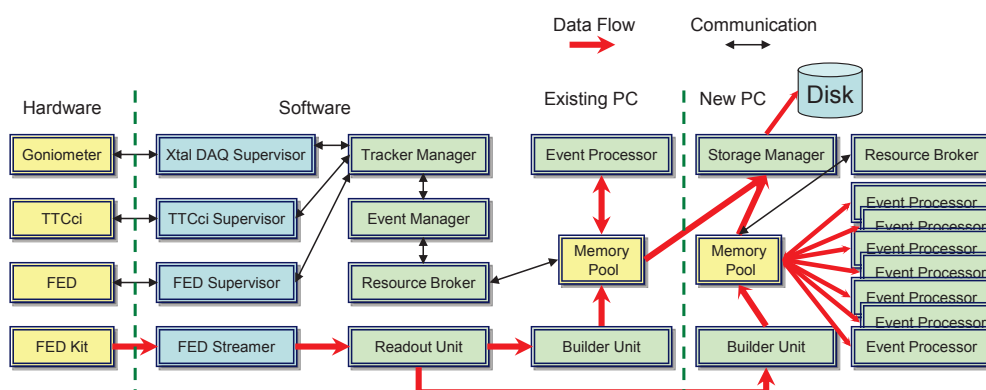


Figure 8. Second version of DAQ software with seven additional Event Processors and their Storage Manager on a new PC. The original Event Processor is used to select a subset of events for data quality monitoring and online analysis.

3.3 Data throughput

The DAQ system readout rate is limited by several factors, the most important being maximum APV trigger rate (140 kHz), FED output data transmission (640 MB/s over S-Link64), FEDKit event to memory (~ 500 MB/s), the number of DAQ PC processor cores available to perform event processing and analysis (which requires from 4 to 7 ms per event per core depending on the speed of the processor) and the event rate to disk (~ 30 MB/s) per disk controller and SM application.

In the case of a small system with only one FED, the bottlenecks are the number of processor cores for event processing and the storage rate to disk. With an event size of 1 kB the maximum rate to disk is expected to be 30 kHz. However, at the outset the DAQ contained only one EP core running at 7 ms per event permitting an average trigger rate of 143 Hz. With the spill structure of 10 s flat top and 45 s period, the in-spill instantaneous readout rate expected is $4.5 \times 143 = 643$ Hz, provided there are no other bottlenecks. With the hardware initially at our disposal it was not pos-

sible to improve upon this trigger rate. Subsequently more PCs were added to the DAQ, including one specialized processor PC with 8 faster cores each capable of processing individual events in 5 ms. The addition of 8 cores allows to run with a configuration including 8 EPs, which increases the peak readout rate to ~ 7 kHz.

Either the addition of more DAQ PCs or a change to the EP architecture is being investigated in order to improve readout rates further. To achieve a peak rate of 40 kHz at least two disk controllers and SM applications would be required and either 45 EPs running at 5 ms per event, or a factor of 5.5 improvement in the processing time per event.

3.4 Data storage and formatting

The FED can be operated in a number of readout modes[8], of which only two are used for telescope operation. One mode outputs the complete raw digitized analogue APV frames and is called *virgin raw*; the alternative is a compressed mode containing only data for hits above a defined charge threshold called *zero suppressed* mode.

The standard operational mode for the telescope FED is in *zero suppressed*. In this mode the data volume is kept to a minimum enabling faster throughput and higher trigger rates. Event data packets formatted in this mode are generally a factor 60 smaller than their *virgin raw* counterpart, which, in the case of CMS, results in a considerable increase in the trigger rate. However, in the case of a small system such as this the improvement is somewhat reduced by a framework packaging overhead that typically adds ~ 1 kB of header information per event. The actual FED data for the telescope are no more than 50 B each in *zero suppressed* and 2.5 kB in *virgin raw* thus giving a reduction in event size from ~ 3.5 kB to ~ 1 kB under default operation.

Following the packaging of the FED data into events, data are then processed and formatted within the XDAQ online framework. Events are stored in the standard CMS data format so that they can be processed both online and offline using the CMS software environment[16] (CMSSW). Since the CMSSW framework is both flexible and modular, standard strip tracker reconstruction packages previously developed and proven by the CMS community can be merged with reconstruction packages written specifically for use with the telescope. The system is also configurable enough so that the entire offline reconstruction can run online. For example, part of the offline reconstruction takes place on a single EP dedicated to data quality monitoring and prompt analysis. The web browsable quantities described in Figure 7 are generated by this module in real time.

4. Results

The silicon microstrip telescope was tested in the CERN H8 beam line in September 2010. The layout of the telescope for this run is described in Figure 9. The upstream section of the telescope for the measurement of incoming tracks is formed by planes 1 and 2 while outgoing tracks are measured using planes 3, 4 and 5. The upstream and downstream sections both have lever arms of ~ 10 m while the goniometer, on which the crystals under test are placed, is situated in between planes 2 and 3. Plane 4 is a rotated XY plane (45°), used in order to resolve ambiguities in reconstruction from multiple outgoing tracks. Events were triggered on the coincidence of signals from a pair of plastic scintillators placed downstream of the telescope.

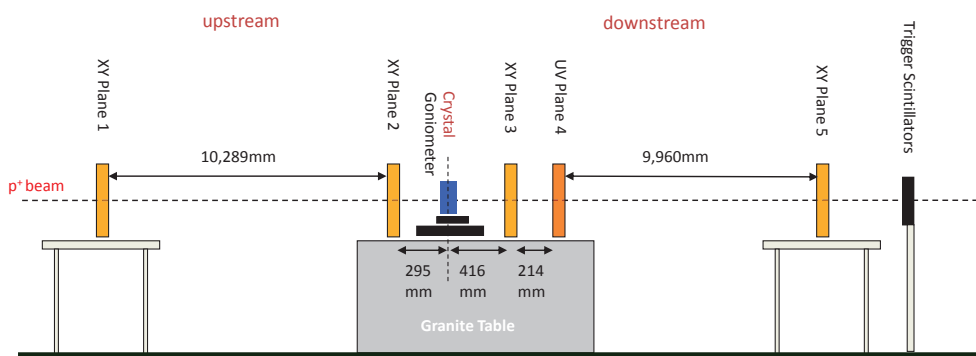


Figure 9. Experimental layout in the H8 beam line. The UV plane denotes the rotated (45°) XY plane.

In this configuration, the dominant contribution to the angular resolution is expected to be from the multiple scattering due to the sensors while the position resolution of the sensors closest to the crystal should determine the impact parameter resolution at the crystal.

4.1 Detector setup and performance

Hit finding is performed both online during zero suppression on the FED and offline as part of the event reconstruction. Using the trigger logic module to provide a fake trigger and with the FED operating in *virgin raw* mode, dedicated runs without beam were used to determine the pedestal and noise values for each strip in the system. A set of pedestals for one sensor, determined using the mean of the signal distribution for each strip, is presented in Figure 10.

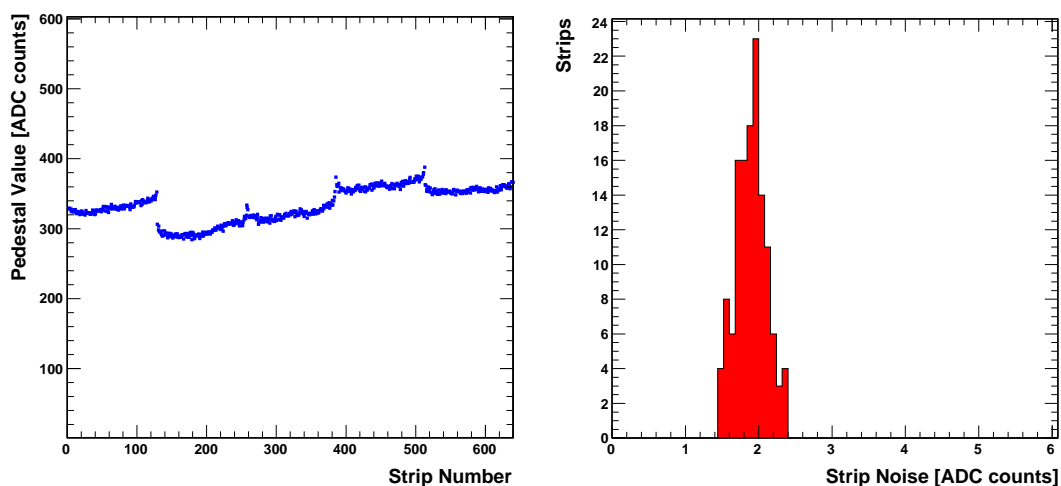


Figure 10. Left: example pedestal values per strip for one sensor (plane 1 - horizontal sensor), and; Right: a typical strip noise distribution (all strips) for a single APV (APV 3) in the same sensor. The noise distribution varies between APVs depending on the relative gain from both the optical links and from the APV itself.

Also shown is a typical noise distribution for one APV in one sensor, defined as the spread of the signal distribution for each strip. The average strip noise in the system was measured to be ~ 2.5 adc counts. After pedestal and common mode subtraction, the FED zero suppression algorithm selects hits as any strip with a signal over noise threshold of 2 to be then grouped into multi-strip clusters unless the signal strip is completely isolated, in which case a threshold of 5 times the noise level is required.

Cluster candidates are defined offline during event reconstruction around seed strips with $S_s/N_s > 3$, where S_s is the signal amplitude and N_s the r.m.s. noise of the relevant channel. Adjacent strips are included in the cluster if they satisfy $S_s/N_s > 2$. Candidates are accepted if the total cluster signal $S = \sum S_s$ is more than 5 times the cluster noise N_c , where $N_c = \sqrt{\sum N_s^2}$. The shorthand ‘3/2/5’ summarises the threshold cuts used in this way. Figure 11 shows the distribution of cluster signals for one APV in a single sensor, following the characteristic Landau form.

To ensure that the sequencer delay is correctly timed to correspond to the peak of the pulse shape stored in the APV pipeline, the programmable delay implemented in the sequencer module can be varied in steps of 25 ns to measure the effect on the cluster signal. Although the beam arrival was asynchronous with respect to the sampling clock, it was not critical to set the delay to precisely coincide with the peak of the APV pulse; it is adequate for the sampling to be within 25 ns after the peak. Because of the slowly varying amplitude of the pulse near maximum only a small error in signal magnitude results. Figure 11 demonstrates how the APV pulse shape can be reconstructed by performing a Landau fit to the cluster signal distribution and estimating the most probable cluster signal over a range of latencies. The optimal delay was determined to be 300 ns after a further ± 25 ns had been applied to the furthest upstream (downstream) sensors in order to account for particle time-of-flight.

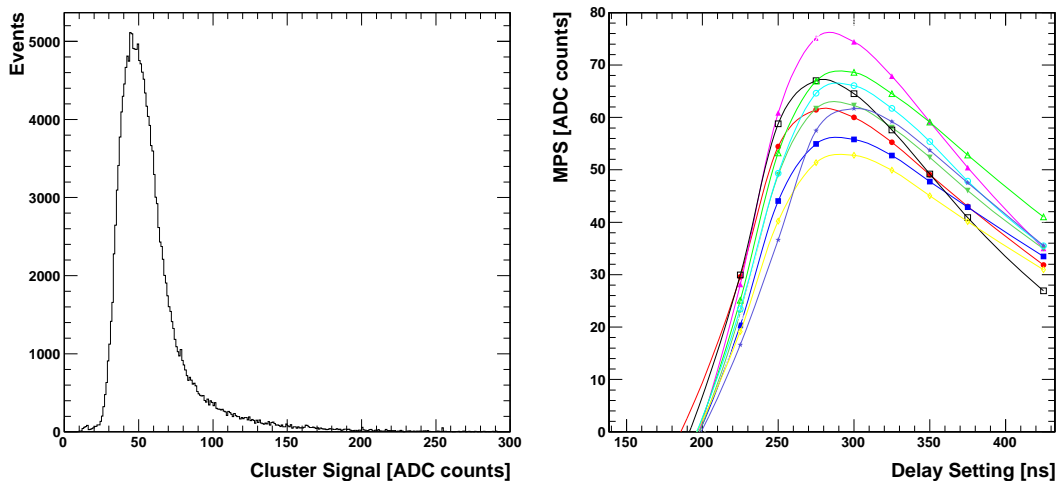


Figure 11. Left: Distribution of cluster signals from a single APV in sensor 2 (APV 3, plane 1 - horizontal sensor) with threshold cuts 3/2/5 with a most probable cluster signal (MPS) of 63 adc counts. The signal distribution may shift between APVs depending on the relative gain from both the optical links and from the APV itself, and; Right: Reconstructed APV pulse shape determined from latency scans for all 10 sensors.

The mean S/N values for all 10 sensors, where N is defined as the average noise level of the strips within the cluster ($N = \sqrt{\sum N_s^2 / n}$), are provided in Table 1. The average value of ~ 32 compares favourably with the measured S/N of CMS modules with similar length strips[1]. There are approximately 1.05 clusters per sensor per event, indicating good performance.

The hit position is estimated using an interpolation of the charge sharing between strips. The charge sharing can be measured by selecting the pair of adjacent strips within the cluster with the greatest signal and defining the variable η ,

$$\eta = S_R / (S_L + S_R) \quad (4.1)$$

where S_L and S_R are the signals on the left and right strips respectively. For the purposes of this telescope, one can estimate the hit position using the linear approximation $d = p\eta$ where d is the position of the hit from the first strip (S_L) and p is the readout pitch. For single strip clusters, the hit position is calculated by assigning $\eta = 0$. A hit is defined from clusters with a width of 4 strips or less.

The cluster width distribution for all sensors is provided in Figure 12. Since the sensors are normal to the beam, single strip clusters are expected to make up a significant fraction of hits. However, the presence of an intermediate floating strip enhances the effect of charge sharing between strips and hence $\sim 65\%$ of clusters are more than 1 strip wide. With the method of interpolation described above, this results in an effective halving of the resolution at the very least since, for example, tracks intersecting the sensor near a floating strip will generate 2 strip clusters while tracks passing in the vicinity of a readout strip are likely to generate 1 strip clusters. A measurement of the sensor resolution is given in Table 1.

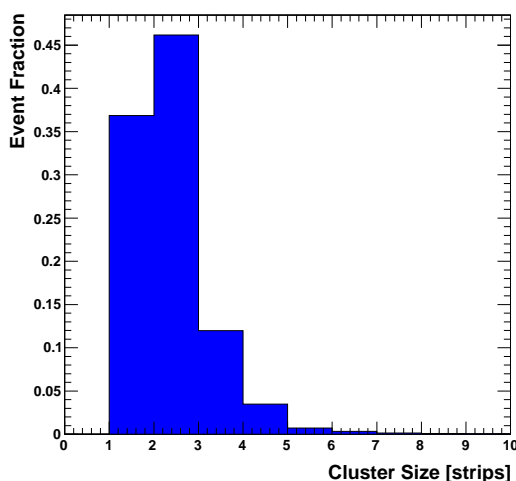


Figure 12. Cluster size distribution for all sensors. The fraction of multi-strip clusters is enhanced with the presence of the intermediate floating strip.

A track based software alignment procedure is used to calculate possible misalignments between sensors. After each intervention in the beam area, dedicated runs were used to collect a

sample of $\sim 100,000$ tracks before the alignment parameters were extracted from the data off-line. Only events with a single hit in each sensor are selected.

Since the detectors are well separated, the procedure must account for the relative offsets in the plane transverse to the beam. Using the first and last planes as a reference, straight line tracks in both coordinates are interpolated to the intermediate planes and the hit residuals are measured. Hits from plane 4 must be rotated -45° about the z -axis. The (x,y) origin of the system is chosen to lie in the centre of the beam spot, while an offset is applied to the last plane so that the average track direction is zero. Iterative corrections are made to the alignment parameters until the residual distributions are centred about zero.

Rotational misalignments of the sensors about the z -axis can also worsen the effective resolution of the detectors. The effect of a rotational misalignment amounts to an interdependence between the impact point of the track along the strip direction and the estimated hit position. Figure 13 demonstrates the correlation between the hit residual along the x -coordinate and the impact point of the track in the y -direction for one particular sensor. The rotational misalignment (twist angle) of each sensor can be estimated from the gradient of these distributions and thus can be accounted for. Iterative corrections are again applied to each of the twist angles until all the x - y correlations are eliminated. The rotational misalignments within the telescope were measured to vary between 0.1 mrad and 8 mrad.

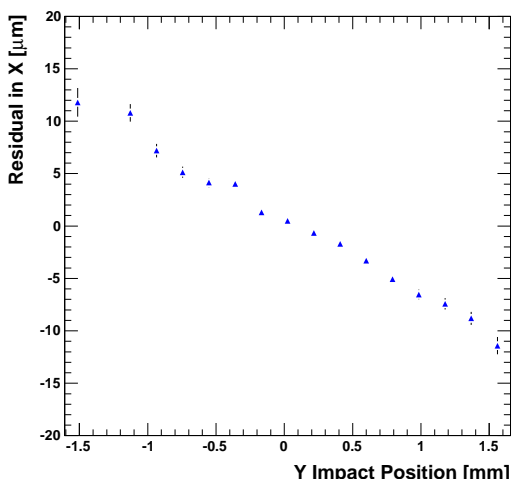


Figure 13. Mean hit residual in the x -projection for plane 3 as a function of the estimated y -impact point on the sensor. The calculated twist angle for this sensor is ~ 7.6 mrad.

The high rates achievable by the DAQ allow the collection of a large dataset within a few minutes. With such high statistic samples, the alignment procedure converges within a few steps and can achieve a precision of $< 1 \mu\text{m}$ for the relative offsets and < 0.1 mrad for the twist angles.

4.2 Track reconstruction and telescope performance

Track fitting for the horizontal and vertical projections proceeds along a similar method to that described in Ref. [17]. Each plane contributes a non-negligible scatter to the track direction and

this error must be combined with the sensor resolution in order to obtain a true measurement error for each x-y point. The track fitting procedure requires at least one hit in each sensor and the z-origin is set at the centre of the crystal.

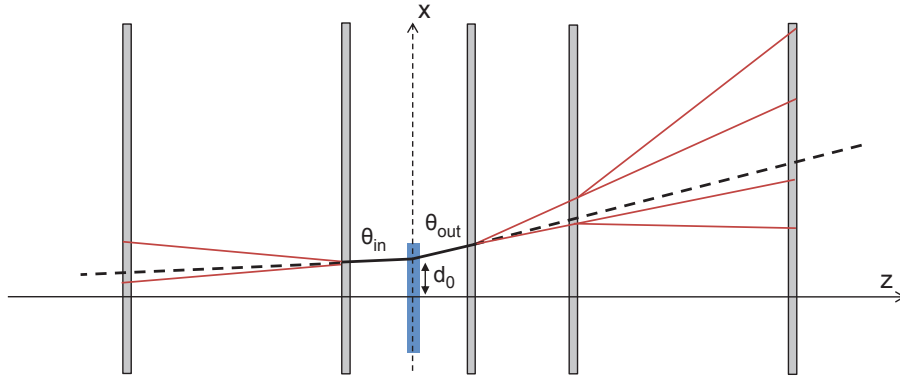


Figure 14. Track fitting method where θ_{in} and θ_{out} are the respective incoming and outgoing angles (solid black lines) at the crystal (blue rectangle) and d_0 is the impact parameter at the crystal ($z=0$). Projections of θ_{in} and θ_{out} are shown by the dashed black lines. Projections of angular errors due to multiple scattering are indicated by the solid red lines.

Since the telescope is required to measure an incoming and outgoing track angle at the crystal, track reconstruction is a minimisation of two straight line fits; between planes 1 and 2 and between planes 3, 4 and 5 where both fits have a common impact point at the crystal origin (Figure 14). As such, there are three free parameters per track per projection which we label θ_{in} (incoming angle) θ_{out} (outgoing angle) and d_0 (impact parameter at $z=0$). With this definition, errors due to multiple scattering must be included in the measurement errors of planes 1, 4 (negligible) and 5. Table 1 lists the estimated measurement errors for each plane including the plane resolutions and calculated errors due to scattering. It has been assumed that each plane contributes $640 \mu\text{m}$ of silicon and $60 \mu\text{m}$ of aluminium, resulting in an angular error per plane due to scattering of $2.4 \mu\text{rad}$ for a $400 \text{ GeV}/c$ proton beam.

The covariance matrix as defined in [17] must also take into account the error correlations between planes due to scattering. For the system described above, the covariance matrix simplifies so that there are only error correlations between planes 4 and 5. As a final selection, a χ^2 cut of less than 10 is placed on the fitted track.

Figure 15 describes the angular resolution of the telescope for both horizontal and vertical projections, measured as the angular deviation between incoming and outgoing tracks ($\Delta\theta = \theta_{in} - \theta_{out}$). Only single track events measured in the absence of the channeling crystal were selected for this analysis. The measured resolutions are $5.2 \mu\text{rad}$ in both x and y. Also shown are the expected distributions from a Monte Carlo simulation of the telescope assuming perfect alignment, $7 \mu\text{m}$ hit resolution and a scattering contribution of $2.4 \mu\text{rad}$ per plane. The ultimate angular resolution of the telescope in this configuration is calculated to be $\sim 4.4 \mu\text{rad}$. The difference can be accounted for by including additional scattering contributions due to the air in the system, in the regions

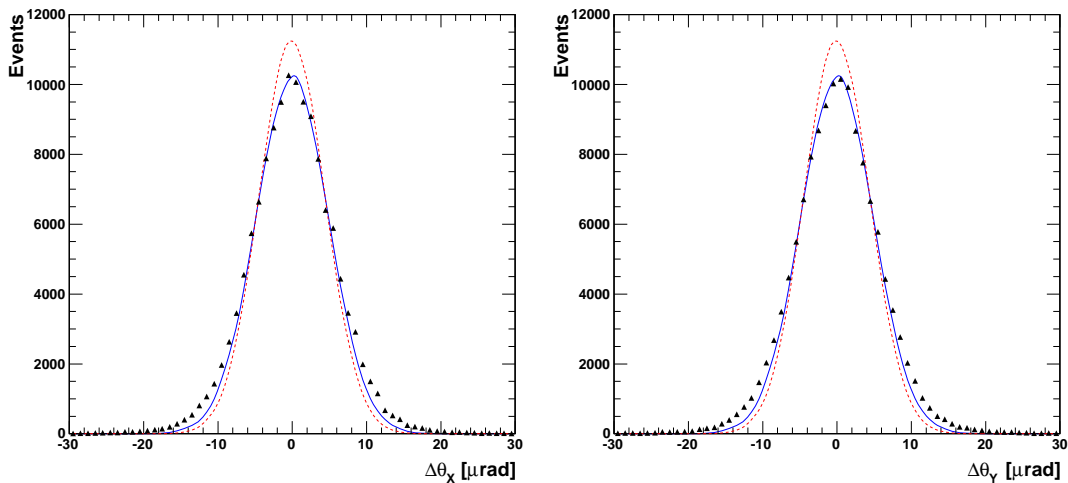


Figure 15. Angular resolution ($\Delta\theta=\theta_{in}-\theta_{out}$) of the telescope in the x (left) and y (right) projections. Simulated angular resolutions neglecting air (red) and including air (blue) are also shown. Non-Gaussian tails are evident, most likely due to delta-rays which are not taken into account in the simulation.

where the vacuum beam pipe could not be extended. The modified simulation estimates an angular resolution of $\sim 5.0 \mu\text{rad}$.

The resolution of the incoming arm of the telescope is particularly significant for channeling applications as it limits how far the effective divergence of the beam impacting on the crystal can be reduced. A highly parallel beam is required for precision channeling measurements and this can be achieved by selecting events where the incoming track is parallel with the the crystalline planes. The angular resolution for the incoming arm has been estimated to be $\sim 2.8 \mu\text{rad}$ from Monte Carlo simulation of the apparatus. This is because the resolution cannot be directly measured unless the incoming beam is known to be non-divergent. The simulation also suggests that the ultimate resolution of the incoming arm is $2.6 \mu\text{rad}$ if air is eliminated from the system.

For this particular application of the detector, it is important to be able to estimate the angular resolution of the telescope. Since multiple scattering is the dominant contributor to the angular error, a measurement of the spatial resolution of the planes is not as significant as it is for conventional telescopes[5]. Nevertheless, the spatial resolution has been estimated using a similar method to [5] for the central three planes where, due to their close proximity, contributions due to multiple scattering can be ignored. In contrast to the track fitting method described above, a simple straight line track fit constituting hits from the central three planes plus either the first or last plane is applied. For each of the central three planes, the detector resolutions σ_d are iteratively varied until the spread σ_p in the pull distributions converge to 1. The pull parameter σ_p is defined as,

$$\sigma_p = \frac{\sigma_r}{\sqrt{\sigma_d^2 - \sigma_f^2}} \quad (4.2)$$

where σ_r is determined from the residual distribution (hit position - fitted track impact position) for the sensor under consideration and σ_f is the impact position error, which is entirely defined by the

covariance matrix and the distances between planes along the z-axis[17]. This method yields an average detector resolution σ_d of $6.9 \mu\text{m}$, where the calculated values are provided in Table 1. This indicates that the sensor spatial resolution is better than the digital resolution of $p/\sqrt{12}=8.7 \mu\text{m}$ where due to the intermediate floating strip, p is given as half the readout pitch.

Plane #	Sensor #	Coordinate	S/N	σ_d (μm)	σ_m (μm)
1	1	x	26.2	-	25.6
1	2	y	26.3	-	25.6
2	3	x	35.0	6.9	6.9
2	4	y	36.0	6.8	6.9
3	5	x	34.6	6.8	6.8
3	6	y	34.5	6.8	6.8
4	7	x	34.9	6.9	6.9
4	8	y	35.4	7.0	7.0
5	9	x	32.1	-	34.8
5	10	y	32.4	-	34.8

Table 1. Telescope sensor parameters, including mapping between sensor number and position coordinate measured. S/N measurements are averaged over all APVs per sensor since chip to chip variations in S/N are small. The detector resolutions σ_d are provided for the central three planes, while the estimated measurement resolutions σ_m are used in the track fitting procedure defined in Figure 14.

4.3 Beam quality and observation of channeling

The telescope was successfully used to characterise the H8 beam before crystal channeling measurements were performed. The beam spot was measured to be roughly Gaussian with a spread of 1.0 mm in x and 0.8 mm in y (Figure 16). The angular divergence of the beam at the crystal, defined as the spread in θ_m , can be measured using planes 1 and 2.

For efficient data taking, it is important that the angular divergence of the beam is minimised since the angular acceptance of the crystal for channeling of 400 GeV/c protons is approximately $10 \mu\text{rad}$. Both the scattering contributions from planes 1 and 2 and the calibration of the beam optics affect the angular divergence. The spread was measured to be $10.7 \mu\text{rad}$ in x and $7.6 \mu\text{rad}$ in y.

One important related effect was observed during offline data analysis. Figure 17 shows that the average θ_m , relative to an initial nominal value, varies with a period equal to the beam spill (flat-top) period. The blue dashed lines indicate the inter-spill beam gap. This effect is observed in every sensor, indicating that the origin is due to some configuration of the beam optics upstream of the telescope. This periodic shift is significant since in order to calculate the crystal properties, tight cuts on θ_m are placed, alongside the requirement that the track must impact on the crystal surface. The telescope is able to resolve that the beam direction shifts by approximately $6.5 \mu\text{rad}$ in x and $2.5 \mu\text{rad}$ in y over the course of a spill. With such a large deviation in the channeling (horizontal) plane, a limited amount of data is useful for analysis. The observation of this effect may also have a consequence on previous measurements of crystal channeling at H8.

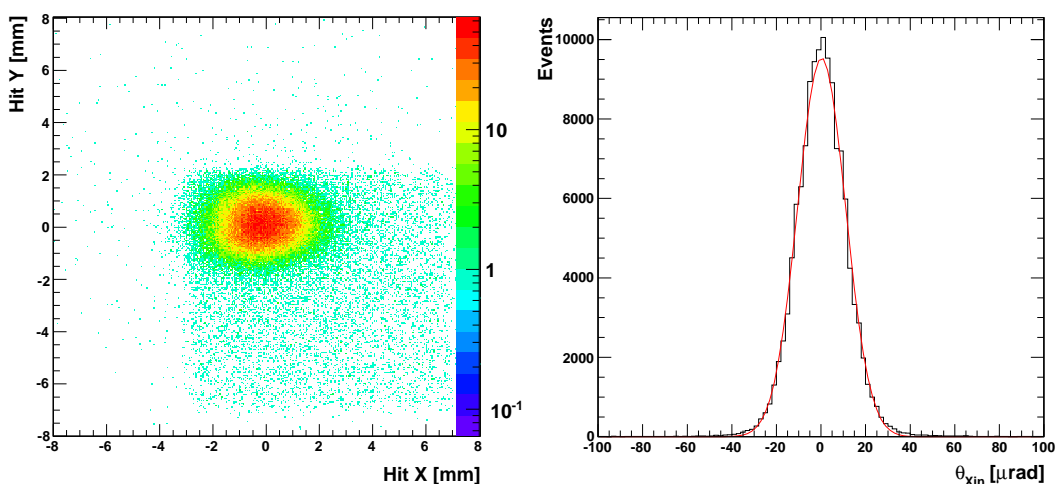


Figure 16. Left: 2-D intensity plot of the measured beam spot incident on the first plane. The non-Gaussian background is due to inefficient beam collimation upstream of the telescope, and; Right: distribution of θ_{in} in the x-projection, giving an estimated divergence of the beam as $10.7 \mu\text{rad}$.

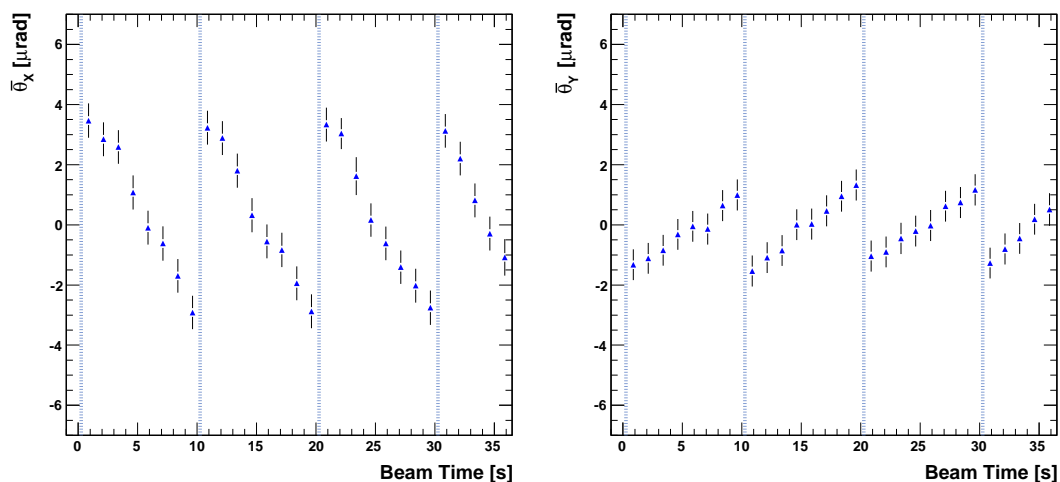


Figure 17. Relative average beam direction $\bar{\theta}_{in}$ in the x (left) and y (right) projection as a function of beam time relative to the beginning of a spill. Blue dashed lines indicate the presence of the inter-spill beam gap of approximately 35 s duration. Beam direction shifts $6.5 \mu\text{rad}$ in x and $2.5 \mu\text{rad}$ in y over the course of a spill.

The beam telescope was successfully used in H8 to qualify and investigate crystals for the UA9 experiment. Detection of the channeling effect for one particular crystal using the telescope is demonstrated by Figure 18 which plots the deflection angle ($\Delta\theta = \theta_{in} - \theta_{out}$) for single track events where tracks are incident on the crystal and when the crystal is in the channeling orientation relative to the beam. An additional cut on the incoming track angle of $\pm 5 \mu\text{rad}$ in the horizontal direction

is placed to reject the tracks that lie outside the critical angle for channeling. A full description of the properties of bent crystals and the channeling of relativistic charged particles is given in Ref. [2]. However, for the purpose of demonstrating the performance of the telescope, Figure 18 shows a clear separation between tracks which do not undergo full channeling but are *volume reflected*[2] with a small deflection angle of $\sim 11 \mu\text{rad}$, and channeled particles which are heavily deflected in the opposite direction at an angle of $\sim 213 \mu\text{rad}$. Both phenomena can be observed in the same set of data because of the finite angular divergence of the beam as well as, as discovered during these measurements, the variation in the incident angle of the beam during a spill. The resolution on these measurements is given by the angular resolution of the telescope, estimated in the previous section to be $5.2 \mu\text{rad}$.

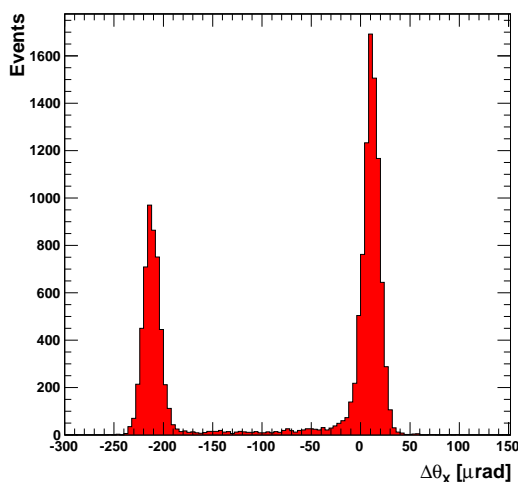


Figure 18. Observation of the channeling effect in the beam telescope indicating a clear deflection ($\Delta\theta = \theta_{in} - \theta_{out}$) of the incident beam. The peak at $-213 \mu\text{rad}$ corresponds to particles which are *fully channeled* by the crystal while the peak at $+11 \mu\text{rad}$ corresponds to particles which undergo *volume reflection*[2].

5. Conclusions

A silicon microstrip tracking telescope for high rate data taking has been constructed and its performance has been estimated at the CERN H8 beam line. The telescope has also been used successfully to measure the trajectories of 400 GeV/c protons through bent crystals to allow the study, with high accuracy, of channeling phenomena as part of the UA9 experiment.

The sensors were found to offer good signal-to-noise performance and an average spatial resolution of $6.9 \mu\text{m}$ per sensor. The setup provides an excellent $5.2 \mu\text{rad}$ angular resolution on the deflection angle of traversing particles. The readout system is largely based on that of the CMS Tracker which has been used to maximise the data acquisition rate. This has been put to good effect as a total of 12 crystals were characterised in a data taking period of one week. It has been observed since that the H8 beam shifts its trajectory periodically; the telescope has measured this deviation to be $6.5 \mu\text{rad}$ in x and $2.5 \mu\text{rad}$ in y over the course of a spill. This is an important effect which should be suppressed in future tests if data taking efficiency is to be maximised.

Acknowledgements

We gratefully acknowledge financial support from the UK Science and Technology Facilities Council. The work would not have been possible without outstanding support from the Imperial College High Energy Physics electronics and mechanical workshops, especially Sarah Greenwood, Maria Khaleeq, Vera Kasey, David Clark and Ian Clark. The support of Lenny Spiegel and Ron Lipton at Fermilab was vital in providing the excellent sensors. We are also grateful to Jan Troska, Francois Vasey, Duccio Abbaneo, Imtiaz Ahmed, Bruno Checcucci for providing CMS components.

We thank all our UA9 collaborators, especially Jerome Lendaro, Frederic Loprete, Alessandro Masi and Walter Scandale for their help in expediting the installation and operation of the telescope apparatus, Gianluca Cavoto and Daniele Mirachi for providing and installing the scintillation trigger and Yury Gavrikov for his expertise in the operation of the goniometer and the alignment of the crystal and telescope.

References

- [1] The CMS Collaboration, S. Chatrchyan et al., *The CMS experiment at the CERN LHC*, 2008 *JINST* **3** S08004.
- [2] W.Scandale et al., *First results on the SPS beam collimation with bent crystals*, Phys. Letters B **692** p78-82 (2010).
- [3] W. Scandale et al., *Apparatus to study crystal channeling and volume reflection phenomena at the SPS H8 beamline*, Rev. Sci Instr **79**, 023303 (2008).
- [4] G. Hall., *Innovations in the CMS Tracker Readout Electronics*, in *At the Leading Edge: The ATLAS and CMS LHC Experiments*, D. Green (ed.), World Scientific 2010, p205-232.
- [5] T. Maenpaa et al., *Silicon beam telescope for LHC upgrade tests*, Nucl. Instr. & Meths **A593**, p523-529 (2008).
- [6] M. Demarteau et al., D0 note (2003) 4308.
- [7] M. French et al., *Design and Results from the APV25, a Deep Sub-micron CMOS Front-end Chip for the CMS Tracker*, Nucl. Instr. & Meths **A466**, p359-365 (2001).
- [8] J. Coughlan et al., *The CMS Tracker Front-End Driver*, 9th LECC Workshop (2003), CERN/LHCC/2003-055.
- [9] J. Troska et al., *Optical readout and control systems for the CMS tracker*, IEEE Transactions on Nuclear Science **50-4**, p1067-1072 (2003).
- [10] J. Varela, *CMS L1 Trigger Control System*, CERN (2002), CERN/CMS-NOTE/2002-033.
- [11] The CMS Collaboration, G.L. Bayatian et al., *The Trigger and Data Acquisition project, Volume I, The Trigger Systems*, CERN CMS TDR 6.1 (2000), CERN/LHCC/2000-038.
- [12] S-LINK Specification, <http://www.cern.ch/HSI/s-link>.
- [13] V. Brigljevic et al., *FEDkit : A Design Reference for CMS Data Acquisition Inputs*, 9th LECC Workshop (2003), CERN/LHCC/2003-055.
- [14] A. Racz et al., *CMS data to surface transportation architecture*, 8th LECC Workshop (2002), CERN/LHCC/2002-034.

- [15] The XDAQ Framework, <https://svnweb.cern.ch/trac/cmsos>.
- [16] The CMS Collaboration, *CMS Physics Technical Design Report Volume 1: Detector Performance and Software*, CERN/LHCC (2006), CERN/LHCC/2006-001.
- [17] M. Penta et al., *Multiple Scattering Error Propagation in Particle Track Reconstruction*, (1994), [hep-ex/9406006].